Applied Surface Science 716 (2026) 164623

Contents lists available at ScienceDirect

Applied Surface Science

journal homepage: www.elsevier.com/locate/apsusc

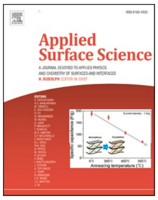

Full Length Article

Near-surface processes of beam-sensitive materials under low energy electron irradiation

Ibrahim Hameli [a,b,c], Vasyl Shvalya [a], Neelakandan M. Santhosh [a], Ardita Kurtishaj Hamzaj [a,b], Oleg Baranov [a,d], Uroš Cvelbar [a,b], Janez Zavašnik [a,b,*]

[a] *Department of Gaseous Electronics (F6), Jožef Stefan Institute, Jamova cesta 39, SI-1000 Ljubljana, Slovenia*
[b] *Jožef Stefan International Postgraduate School, Jamova cesta 39, SI-1000 Ljubljana, Slovenia*
[c] *Department of Physics, University of Prishtina "Hasan Prishtina", George Bush 31, 10000 Prishtina, Kosovo*
[d] *Plasma Laboratory, National Aerospace University, Kharkiv, Ukraine*

ARTICLE INFO

Keywords:
Electron irradiation
Electron beam interactions
Beam sensitivity
Gold chloride
Carbon deposition
Nanostructure formation

ABSTRACT

We investigate the interactions and modifications induced by low-energy electron beam irradiation in beam-sensitive materials, with crystalline gold trichloride ($AuCl_3$) as a model system. Employing scanning electron microscopy (SEM) coupled with energy-dispersive X-ray spectroscopy (EDS) in an *operando* setup, we investigated surface and bulk transformations as a function of irradiation time (0–1080 s) and accelerating voltage (1–30 kV). Irreversible structural changes were observed both on the surface and within the bulk of the $AuCl_3$ crystal. Surface analysis revealed the formation and growth of μm-sized vertically oriented carbon nanopillars, with voltage-dependent growth dynamics governed by backscattered (BSE) and secondary electrons (SE). At the same time, the bulk of the $AuCl_3$ decomposed under carbon pillars, forming Au nanoparticles and near-surface voids whose size and spatial distribution correlated with the energy deposition profiles. The observed morphological and chemical alterations pose a significant obstacle to accurate chemical composition analyses by energy-dispersive X-ray spectroscopy (EDS) and suggest a narrow operating window for conducting reliable SEM analysis.

1. Introduction

Electron microscopy of beam-sensitive materials presents a significant challenge due to the rapid structural damage caused by the electron beam and associated issues. Low-energy electrons (1–30 keV) can cause radiolytic damage [1], degradation (knock-on displacement [2] and damage by the induced electric field [3–5]), heating [6], and charging in materials such as zeolites nanosheets [7], metal–organic frameworks, carbon nanotubes [8], semiconductors [9], organic–inorganic hybrids and exceptionally soft, porous poorly conducting low density and polymer materials [10–12]. Radiolysis is the predominant damage mechanism in thin organic specimens. In contrast, knock-on displacement is the primary mechanism for conducting inorganic specimens and high-Z materials, which require an extremely high electron dose ($>1000\ C/cm^2$) and energies beyond the capabilities of SEM systems [13]. In low-voltage SEM systems, dynamic charging is another problem caused by changes in the leakage resistance of the sample under electron irradiation [14]. This low-keV e-beam irradiation can also lead to charging of wide-bandgap materials, which can influence the development of radiation damage, defect migration [15,16], surface diffusion phenomena, and the trapping of charges beneath the surface [17]. Most reports focus on damage caused by low-energy beams, which is limited to the sample surface, while less data is reported on the material's bulk structure and integrity. Therefore, the combined quantification of beam damage, visualizations, and characteristic doses is crucial for optimizing the analysis of beam-sensitive materials and for potential electron beam modification of the material [7,18].

Alongside charging, electric field damage, and radiolysis, the local carbon deposition is a frequently observed phenomenon in SEM [19,20]. It is generally accepted that the volatile carbon-rich organic molecules come from diffusion from the metal walls, gaskets, and greases, outgassing of metal parts exposed to the electron bombardment, and from a sample's surface and sample fixation materials [21,22]. The deposition of carbon in SEM is caused by chemical reactions between organic molecules and the electron-bombarded surface, involving secondary electrons [23,24] or X-rays [25]. Typically, carbon deposited on the

---

* Corresponding author at: Department of Gaseous Electronics (F6), Jožef Stefan Institute, Jamova cesta 39, SI-1000 Ljubljana, Slovenia.
E-mail address: janez.zavasnik@ijs.si (J. Zavašnik).

https://doi.org/10.1016/j.apsusc.2025.164623
Received 30 July 2025; Received in revised form 4 September 2025; Accepted 12 September 2025

sample's surface increases with total electron dose but can be minimized by high beam current and short illumination time. If knock-on damage is not an issue for a subjected material, the electron energy should be maximized to reduce such deposition [19]. Carbon deposition on the sample surface can physically change the size of the measured features and reduce image contrast, potentially introducing significant dimensional metrology errors and chemical composition analysis [26]. Both low-keV damage to beam-sensitive materials and associated carbon pile-up can influence not only visualization but also affect quantitative compositional analysis by EDS, particularly when the beam is focused on a nanometric area for an extended period. On the other hand, carbon polymerization on the sample surface can be utilized, as demonstrated by high-aspect-ratio nanoscale C-tips for low-capillary-force probes in atomic force microscopy [26] and as nano-sized field emitters for electron guns [26], which illustrates a new approach for designing functional nanodevices.

Currently, there is no reliable data connecting surface and subsurface transformations and visualizing what is happening in the bulk of the material under beam irradiation. Are these processes happening simultaneously, and what are their dynamics? To understand the damage mechanism, the conditions under which it occurs, its consequences, and to facilitate the use of nanocarbon engineering strategy, we designed a specific experiment to tackle both challenges. With special attention to the accelerating voltage and exposure time, we irradiated a member of the transition metal chlorides, a beam sensitive $AuCl_3$, to investigate possible dynamics of carbon pile-up during *operando* EDS spot analysis, its effect on detected chemical composition data, and the effect of the low-keV e-beam on the internal stability of a bulk crystal. Using this approach, we found that the carbon pillars grow both vertically and horizontally, with their bases being wider at lower voltages, and exhibit reasonable control over their height over time. However, the carbon pillars strongly affect the chemical composition results by EDS. Furthermore, during prolonged exposure, the bulk $AuCl_3$ decomposed, accompanied by associated mass loss, the formation of Au nanoparticles (Au NPs), and the creation of nanovoids. The spatial dimensions of voids correlate well with the decrease in the Cl/Au atomic ratio and the calculated deposited energy profile, suggesting that the largest voids are expected within the 10–20 keV irradiation window.

2. Materials and methods

2.1. $AuCl_3$ sample preparation and optical properties

Dehydrated powdered $AuCl_3$ (auric chloride, CAS # 13453-07-1, Sigma-Aldrich) was dissolved in deionized water (1 mM). We used the dual-beam UV–Vis spectrometer (PerkinElmer Lambda 1050) with a measured range of 250–850 nm and a resolution of 1 nm to analyze the solution for the presence of Au ions. Afterwards, 1 μL of solution was pipetted on a silicon wafer and dried in a fume hood at ambient conditions. Such a prepared sample consists of $AuCl_3$ crystals formed on the surface of the silicon wafer.

2.2. Electron-beam irradiation study

Electron-beam irradiation experiments were performed using scanning electron microscope (SEM, Prisma-E, Thermo Fisher Scientific, Inc.) equipped with an energy-dispersive spectrometer (EDS). The crystalline $AuCl_3$ on a Si wafer sample was inserted into an SEM chamber and evacuated to a pressure of approximately $1–2 \times 10^{-4}$ Pa. For the electron irradiation experiments, the convergence angle of the electron beam was fixed via condenser lens and aperture settings, corresponding to the spot size (SS) 2.5 parameter with an effective e-beam diameter of approximately 1 nm (see *Supplementary Information File, SI*). The range of acceleration voltages and irradiation times was 1–30 kV and 20–1080 s, respectively, in spot mode at a constant field of view (scan width of 2.54 μm) at a working distance of 10 mm. Before experiments, the electron beam current (I) versus accelerating voltage (U) was characterized by *an in-situ* Faraday cup (see the *SI*). All reported irradiation experiments were performed on the same Au-chloride crystal.

In the first experimental setup, we irradiate the $AuCl_3$ crystal with varying accelerating voltages (3, 5, 10, 15, and 30 kV) for different irradiation times at each spot. In the time range of 20–600 s, the irradiation spots were single-exposed, while spots >600 s were irradiated twice. In the second experimental setup, the irradiation time was kept constant (600 s), combined with the variation of the accelerating voltage (3, 5, 10, 15, and 30 kV), with additional 1, 2, and 20 kV exposures.

The cross-sections of the irradiated $AuCl_3$ sample were made by dual-beam focused ion beam (FIB-SEM, Helios NanoLab 650i, FEI Inc.). To preserve the delicate surface structures, the samples were first sputter-coated with 100 nm of platinum (Pt) using a precision etching coating system (PECS Gatan, plc). In FIB, the selected micro locations were additionally covered with 300 nm of e-deposited tungsten (W), followed by 500 nm of ion-beam-deposited tungsten. Such a thick metal layer deposit successfully protected the Pt-sputtered Au-chloride and surface structures during analysis and cross-section ion milling.

The three main experimental observations in our study — carbon deposition in a pillar shape on the crystal surface, nanovoids, and Au nanoparticles in the sample bulk — are explained using theoretical models proposed by Kanaya-Okayama [27] for energy deposition inside the sample and the Reimer model for thermal effects. The experimental conditions were replicated as closely as possible through simulations of electron beam interaction with the sample, based on Monte Carlo methods run in the CASINO V2.42 codes [28,29]. From simulations, we obtained valuable data on the interaction range, energy distribution in the sample, and interaction products, including backscattering electrons and secondary electron yield. The simulation results are combined with theoretical ones to explain those experimental observations.

3. Results

3.1. UV–Vis and SEM characterization

To confirm the presence of Au^{3+} ions, the $AuCl_3$ solution, diluted to 1 mM in Milli-Q water with a typical yellowish color, was characterized using UV–vis spectroscopy (Fig. 1(a)). We recorded a characteristic absorbance peak at 290 nm [30], which originates from ligand-to-metal electron transitions (Cl 2p to Au 5d) [31]. All the $AuCl_3$ was diluted, and no presence of metallic Au was detected.

The SEM analysis of dissolved $AuCl_3$ droplets dried at ambient conditions on a Si wafer reveals monoclinic $AuCl_3$ crystals, 5–30 μm in size (Fig. 1(b)). The crystal in Fig. 1(c) was used for irradiation studies with a selected beam current profile. The results of beam current versus accelerating voltage measurements, taken using an in-situ Faraday cup, for a fixed selected spot size (2.5 mm) used in the irradiation experiment, are shown in Fig. 1(d). The beam currents measured for different spot sizes are summarized in Table S1, and their respective beam current–voltage (I-U) curves are shown in Fig. S1 of the SI file. These I-U graphs show that the beam current increases from 0.2 to 1 kV, then decreases at 2 kV, and after 3 kV, it increases linearly to 30 kV, reaching a value of 42.2 ± 0.1 pA. We attribute the deviation in the 1–3 kV region to the intrinsic properties of a tungsten filament associated with chemical doping [32].

3.2. The estimation of fluence, electron flux, and absorbed dose

The damaging interaction of electron beams with materials limits the use of electron microscopy in probing biological, polymeric, and other beam-sensitive materials [3]. The maximum tolerable dose, rather than the technical capabilities of the microscope, determines the ability to visualize and image such materials. The studies report that electron-sample interactions employ a variety of techniques and reporting

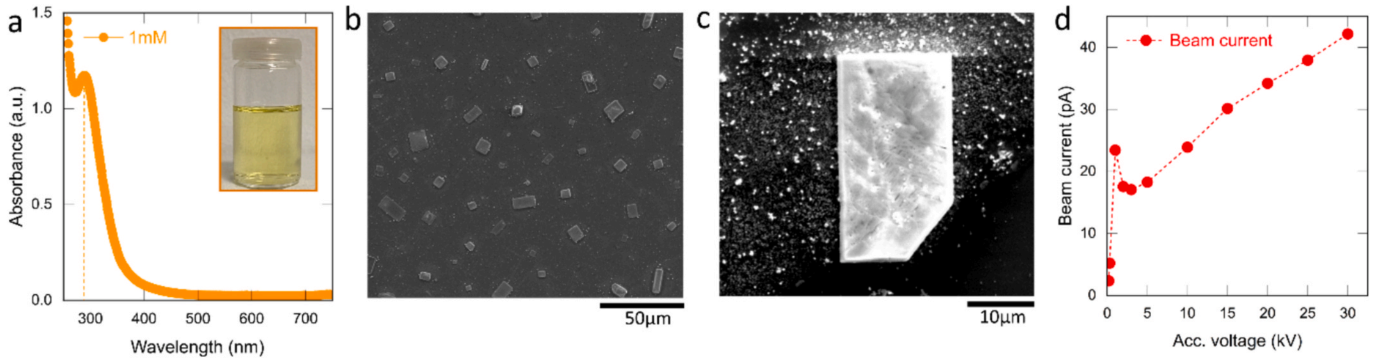

Fig. 1. (a) UV–Vis spectrum of the water diluted (1 mM) precursor; (b) overview SEM micrograph of $AuCl_3$ crystals formed after drying on Si wafer, (c) SEM micrograph of $AuCl_3$ crystal for irradiation studies; (d) I-U characteristic of the electron beam for electron beam conditions used in irradiation experiments (spot size of 2.5).

parameters, such as secondary electron emission and trapped charge [33], as well as other methods, to assess energy deposition over electron energies ranging from eV to the kilovolt range. Differences in beam energy, current density, and exposure timing influence the observed effects, which vary from charging artefacts to localized dose impacts.

The total cumulative dose of electrons received by the sample is the key irradiation parameter that correlates with sample alteration. In electron microscopy, the irradiation dose (number of incident electrons per unit irradiated area) is typically considered simply as the number of electrons received per unit area of specimen, a.k.a. the particle fluence $F = N/A$, where N is the total number of incident electrons, and A is the sample irradiated area. In our case, the fluence estimated for 1 kV is 1.863×10^{26} e^-/m^2, while for 30 kV is 3.352×10^{26} e^-/m^2, which are equivalent to an incident charge density of $2.984 \times 10^7 C/m^2$ and $5.371 \times 10^7 C/m^2$, respectively. Another parameter frequently used in electron microscopy is the rate of electrons passing through an irradiated area, known as the electron flux (the number of incident electrons per unit area per unit time), where F represents the fluence and t represents the exposure time. Again, for 1 kV, the electron flux is 1.863×10^{26} $e^-/m^2 \cdot s$, and for 30 kV, it is 3.352×10^{26} $e^-/m^2 \cdot s$, respectively. In Fig. 2(a), we have shown the electron flux calculated for all spot sizes in the 1–30 kV range.

The above calculations were about the number and intensity of electrons reaching the sample surface. But the electrons in the kV range are very energetic; thus, they will penetrate straight into the sample bulk. Inside the sample, the electrons scatter elastically or inelastically. As the sample damage is due to inelastic scattering, it is advantageous to express irradiation dose in Gray (Gy) units, which quantify the energy deposited per unit mass of the specimen (1 Gy = 1 J/kg) through inelastic scattering, to make the measurement and the resulting radiolysis effects independent of the electron accelerating voltage and enable direct comparison with other methods.

The absorbed dose in SEM is calculated by relating the electron-beam characteristics to the interaction with the sample. However, due to the variation in depth-dose profiles of kilovolt-electrons in the sample, careful attention must be given to the method used for determining the total absorbed dose. The estimation was experimentally determined for electron energy dissipation versus penetration depth in solid materials using the Everhart and Hoff expression [34] and further elaborated upon by Galloway and Roitman [35]. The calculation of the *absorbed dose G* by the sample bulk using normalized correlational coefficients computed from probe current can also be calculated by a simple formula for converting electron fluence F to Gray units, based on a near constancy of the stopping power per electron [36] as:

$$G = SF[Gy] \tag{1}$$

where S is the density-normalized stopping power of electrons ($J \cdot m^2/kg$) during interaction with the $AuCl_3$ sample, and the values are obtained using the Bethe non-relativistic model for stopping power [37]. The results of absorbed dose for several spot sizes, over the 1–30 kV range, are shown in Fig. 2(b). For 1 kV and 30 kV, the estimated cumulative absorbed dose is 3.178×10^{13} Gy and 9.504×10^{12} Gy, respectively. Fig. 2(b) shows that the absorbed dose decreases rapidly in the 1–5 kV range and slower in the higher kV regime, because the inelastic events scale inversely with the e-beam energy [38]. Due to this relation, the e-beam inelastic damage, particularly for sensitive materials, is higher at

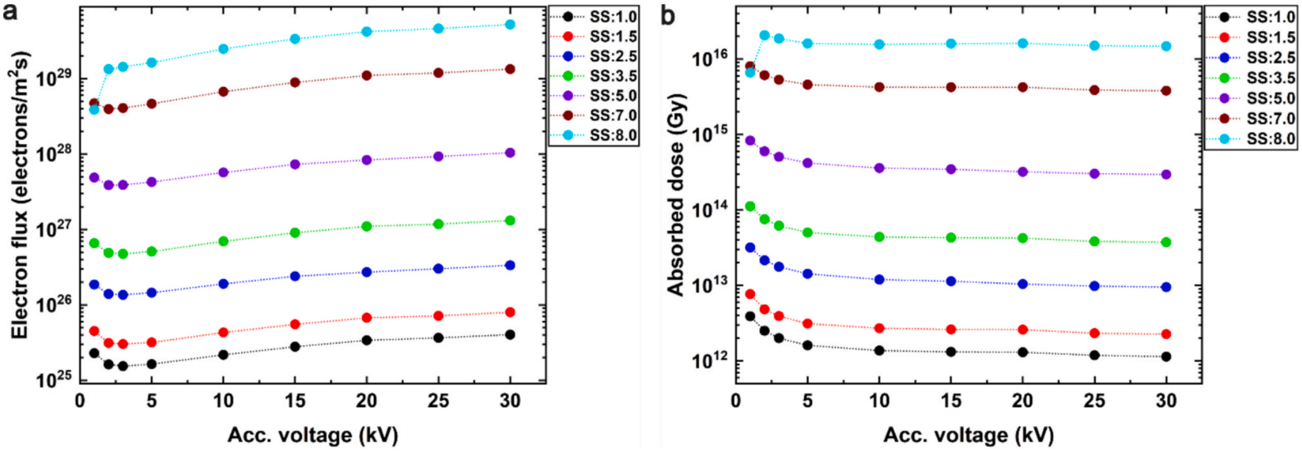

Fig. 2. (a) The variation of electron flux through the sample surface over 1–30 kV for several spot sizes, (b) the cumulative absorbed dose of e-beam inside the sample bulk.

lower e-beam energies. Further, if parameter S in Eq. (1) is multiplied by the electron flux, the result can be expressed as the dose rate (Gy/s), which quantifies the rate of power absorbed by the sample.

3.3. Sample surface alteration after e-beam irradiation

To assess the impact of electron beam irradiation on the surface morphology alteration of the $AuCl_3$ single crystal, we irradiated the sample in spot mode for different kV and exposure times. As shown in Fig. 3(a), the micrograph acquired by the back-scattered electron (BSE) detector reveals circular black features at irradiation spots, with increasing diameter as the irradiation time progresses. Since the BSE detector is highly sensitive to Z-number variation, the black spots are composed of elements lighter than $AuCl_3$, and were identified by EDS as carbon. Secondary electron (SE) micrographs (Fig. 3(b)) reveal in detail the top and tilted surface morphology of nanocarbon formation created with a 3 kV e-beam at different times of irradiation, and the top-views for other kVs are presented in Fig. S2 in Supplementary Information File (SI). The base diameter of the carbon-deposited pillars was measured, and the data are plotted (Fig. 3(c)) for selected cases, namely 3 kV, 5 kV, and 30 kV. Comparing three cases, it is evident that the base of the pillars is smaller at high voltages, which is about twice (1.91) smaller for 30 kV (205 nm) than that observed for 3 kV (392 nm). The growth diameter d is not linear over the full range of irradiation times, showing a clear trend toward saturation, and was fitted with a typical parametric cumulative distribution function: $d\ d_{max}(1 - exp(-\alpha t))$, where α defines the growth rate. The value of this parameter is: $\alpha = 4.4 \times 10^3$ nm/s (3 kV), $\alpha = 3.3 \times 10^3$ nm/s (5 kV), and $\alpha = 3.0 \times 10^3$ nm/s (30 kV), suggesting faster lateral growth of the carbon pillar at lower accelerating voltages. Fig. 3(d–e) shows top and tilted views of carbon pillars grown at the irradiated spots with different kV settings for 10 min, and the corresponding graph is provided in SI, Fig. S3.

3.4. The decomposition of near-surface crystal bulk

The sample irradiations were done in spot mode, and the EDS data for the chemical composition evaluation were recorded simultaneously. The EDS intensity profiles are plotted for 3 kV, 5 kV, 15 kV, and 30 kV, covering an irradiation time range of 20–1080 s, as shown in Fig. 4(a–d). Fig. 4(e–f) shows the variation of X-ray counts for carbon and silicon at different accelerating voltages. These graphs show that the X-ray signal over time tends to deviate from linearity. In the case of carbon intensity, this deviation is due to the in-situ growth of carbon deposition on the sample surface during irradiation. For the silicon case, it serves as a marker for electrons traveling through the sample and reaching the substrate, particularly at high kV. The EDS plots reveal the presence of gold and chloride; however the Cl/Au atomic ratio graph in Fig. 4(g) indicates a decrease in the chloride content in the sample bulk, indicating decomposition of the sample $AuCl_3$ bulk sample.

To investigate the alterations occurring under the sample surface, cross-sections for subsurface analysis were made by focused ion beam (FIB). The SE micrographs shown in Fig. 5(a–d) reveal that the bulk of the sample near the surface is permanently damaged. The near-surface decomposition of the sample crystal results in Au NPs formation (Fig. 5(e)) and mass loss (nanovoids) (Fig. 5(f)). As a result of decomposition, Au atoms coalesce in Au NP while Cl diffuses through the crystal and escapes into the vacuum. The Au NPs with a diameter size of 10 nm or larger are agglomerated, while the most considerable void, under a 10 kV irradiation spot, is 850 nm wide and 520 nm deep.

4. Discussions

4.1. Spatial growth of carbon pillars

Samples subject to microscopy experiments are rarely free of the presence of hydrocarbons. There are multiple possible sources of hydrocarbon molecules, including residual atmospheric gases that

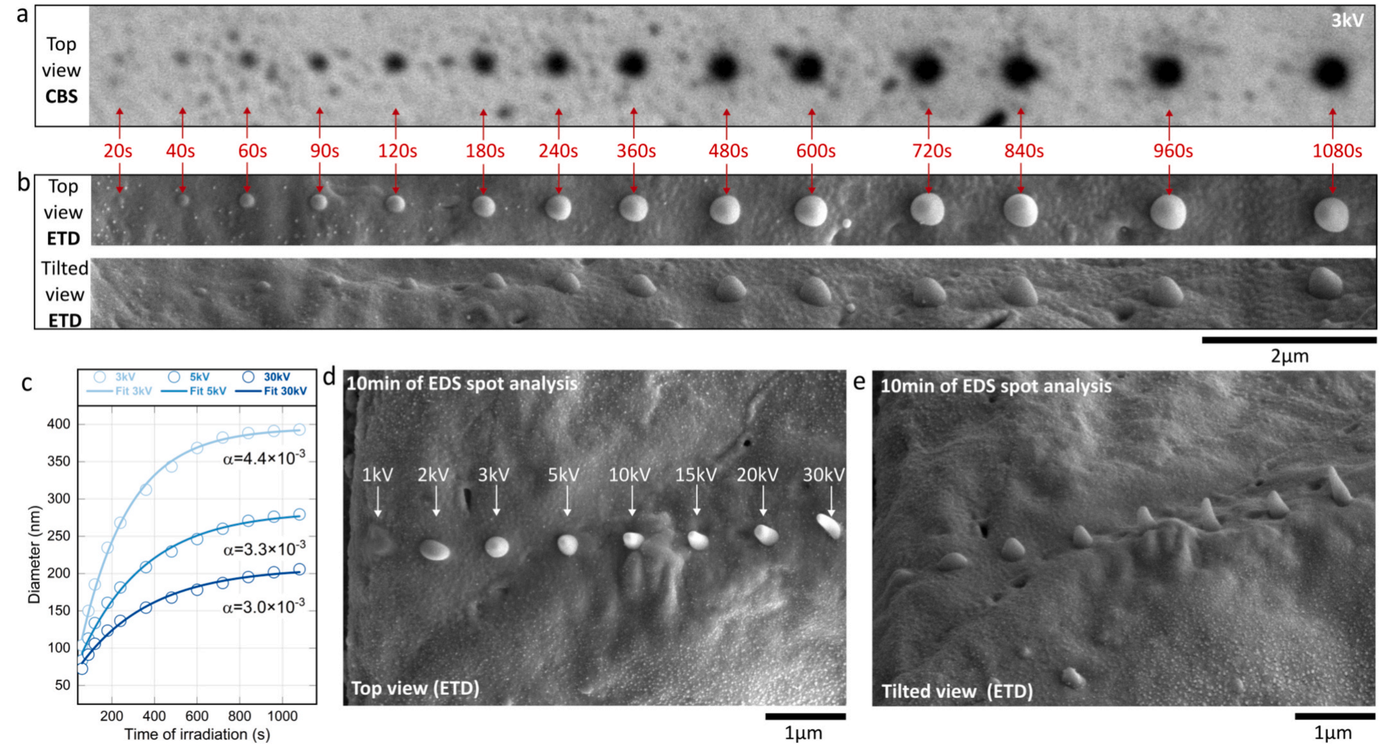

Fig. 3. (a) Top view BSE micrograph of the sequential irradiation of a crystal surface at 3 kV, (b) corresponding top and tilted (52°) SE micrographs, (c) experimental data accompanied with a parametric fit for a base diameter of pillars at selected accelerating voltages as a function of irradiation time, and (d–e) SE micrographs showing of carbon pillars obtained after 10 min of irradiation at 1–30 kV; top and tilted view.

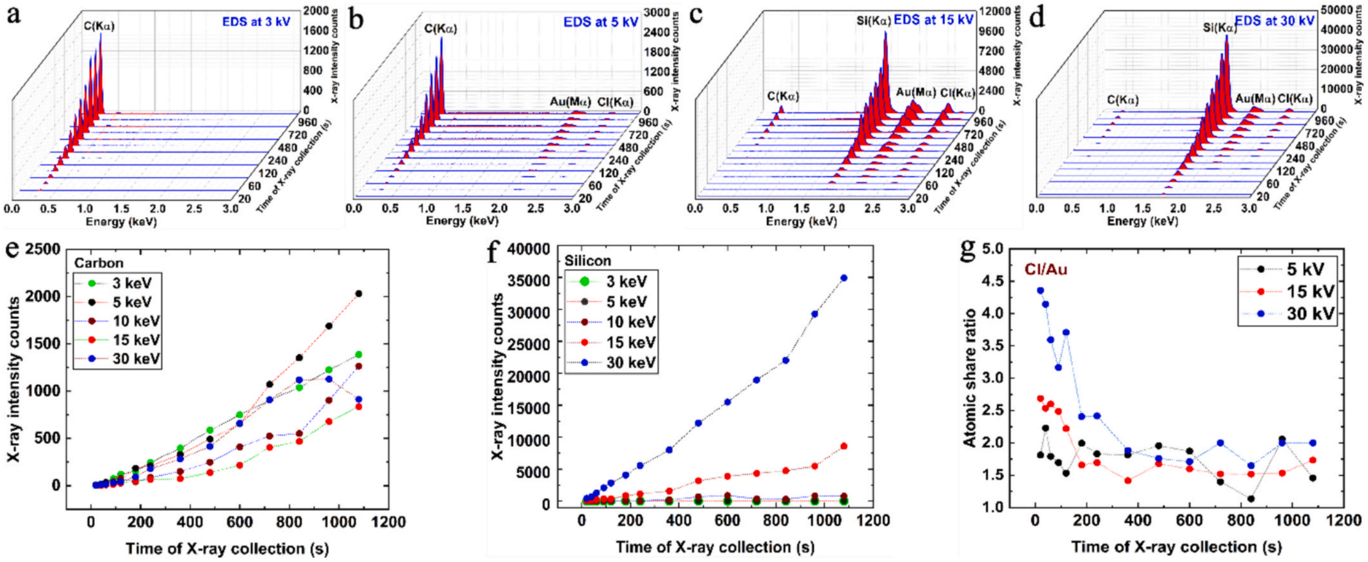

Fig. 4. (a–d) The EDS spectra recorded on the AuCl$_3$ sample at different acc. voltages. (e–f) Temporal X-ray intensity variation for (e) carbon and (f) silicon in the acc. voltage range of 3–30 kV. (g) Temporal Cl/Au atomic ratio variation at 5, 15, and 30 kV.

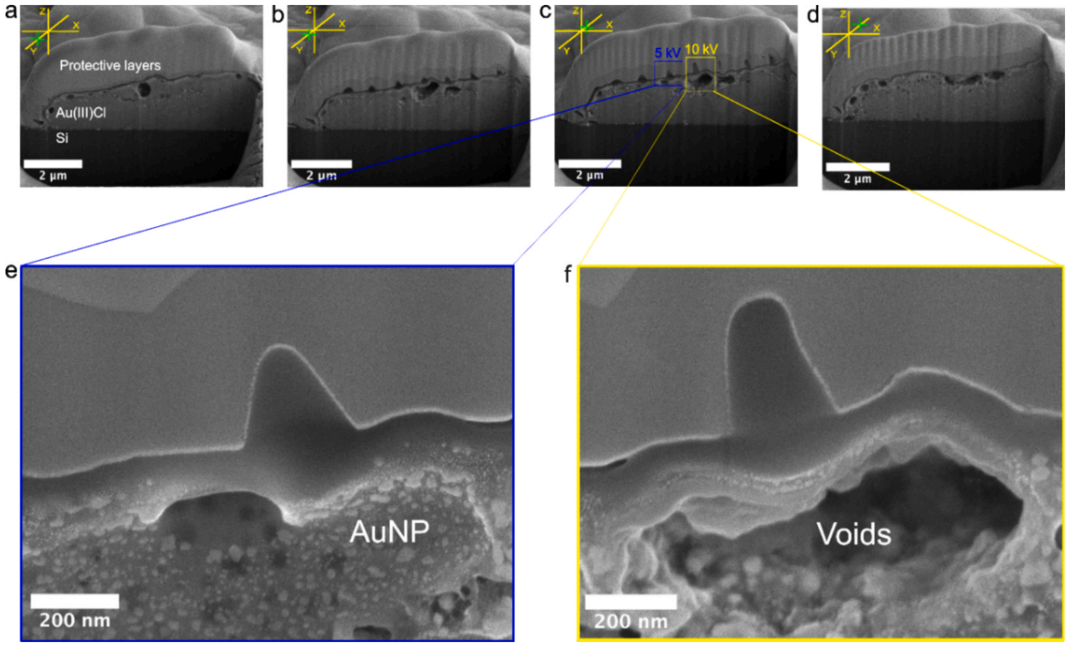

Fig. 5. The FIB cross-section micrographs (a) – before, (b–c) – in, and (d) – after the irradiation spots, with the cuts made in z-x plane after each 100 nm in y direction, (e)- the zoomed area show distribution of Au NPs under 5 kV-pillar near crystal surface, and (f) – zoomed area of largest voids under 10 kV.

originate directly from vacuum pumps, desorption from the inner walls of the microscope chamber, and deposition on sample surfaces during their preparation [19,39,40]. These molecules exist in the gas state or are adsorbed on the sample surface. The hydrocarbon molecules have a dissociation threshold energy in the range of 3–4 eV [41,42], which is easily overcome by primary electron beam, backscattering electrons (BSE), and secondary electrons (SE). The incoming e-beam initiates the dissociation and polymerization of hydrocarbons, with carbon deposition occurring precisely at the spot of irradiation. The spatial growth of C-pillars rapidly exceeds the dimensions of the irradiated area, and their growth dynamics cannot correlate solely with incident electrons. In this regard, electrons ejected inelastically from sample atoms must be considered, particularly the SE energy, which corresponds to the dissociation cross-section peak of hydrocarbons, enabling them to contribute significantly to the growth of the carbon pillars [43]. SE produced directly from the incident beam of electrons are known as SE-I and escape from regions of the sample several nanometres below and around the irradiation spot. BSE originates from a deeper volume of the sample and escapes from much broader areas of the sample, and on its way out, produces other SE, known as SE-II. The elastic and inelastic interaction products of the e-beam with the solid sample occur through an interaction volume with a typical shape, as visualized in Fig. 6(a) via Monte Carlo simulations.

The SE-I escape only several nanometres wider than the irradiation spot diameter. As the C-pillars are much wider than the SE-I escape area, the SE-II must contribute the most. Several studies have connected the growth of the C-pillars with SE [23,24,41,42,44]. Two features of SE make them as suitable mechanism to explain the C-pillars spatial

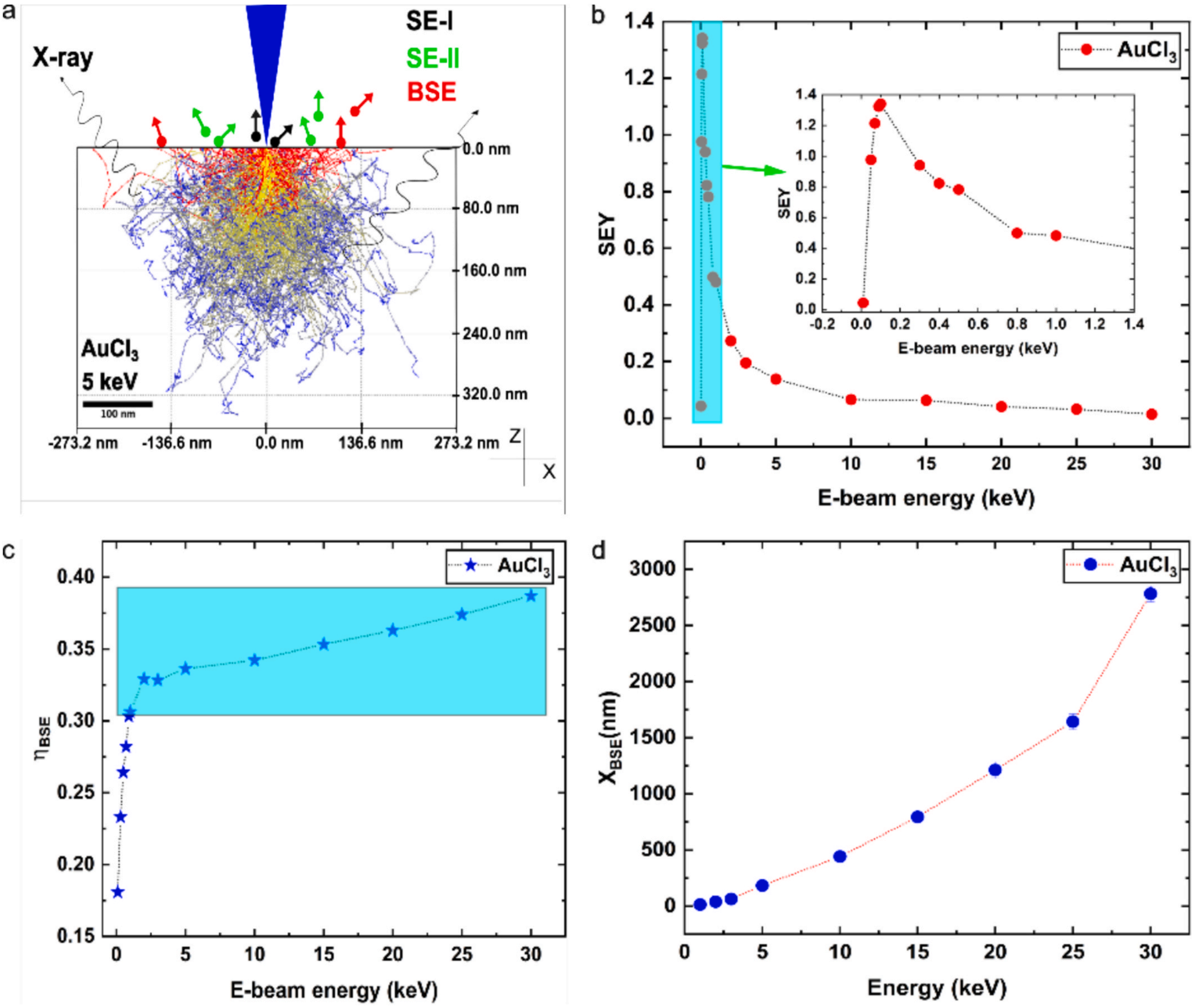

Fig. 6. (a) – The typical shape of e-beam-solid interaction volume. The e-beam trajectories visualization is based on simulations of electron interactions with $AuCl_3$ at 5 keV. The visualization shows an energy profile, with the highest energetic electrons coloured in yellow and shifts to blue at lower energies. In contrast, the red lines show BSE. (b) Secondary electron yield (SEY) of $AuCl_3$ was acquired through simulations, with highlighted area showing the SE yield behaviour around the peak. (c) The BSE coefficient of $AuCl_3$ obtained from simulations with the range of e-beam energy of interest highlighted, and (d) BSE lateral distribution in $AuCl_3$ acquired from simulations.

growth. First, it is their larger escaping area from the sample that explain why the dimensions of carbon deposition dimensions exceeds enormously the e-beam diameter, and secondly, the secondary electron yield (SEY) decreases with increasing keV (see Fig. 6(b)), which explain the C-pillars getting narrower with higher e-beam energy. On the other hand, BSE contributes indirectly, as a provider of SE-II. Fig. 6(c) shows the variation of the BSE coefficient η_{BSE} for $AuCl_3$ over e-beam energy range. It depicts a rapid increase of BSE yield in the range 1–5 keV, followed by a stable trend until 30 keV. Thus, if the width growth of pillars depends directly on BSE, then a wider C-pillar is expected in 5 kV than in 3 kV, which is not what we experimentally observed.

So far, the spatial growth of C-pillars is dependent on SE and BSE emitted from the $AuCl_3$ crystal, but apparently this is not the whole story. The C-pillars are even wider than the SE-II lateral escape area from the sample. Fig. 6(d) shows the average diameter X_{BSE} of lateral escape from the crystal obtained from simulations. The X_{BSE} is narrower than the C-pillar width in low kV. For example, at 3 kV, the carbon pillar width is 301 ± 3.0 nm, while the X_{BSE} is 97.1 ± 2.0 nm. The hydrocarbon decomposition, followed immediately by carbon deposition, is a dynamic process that happens in situ with ongoing irradiation. The interaction of the e-beam with the C-pillars erecting will produce more SE and BSE [24] from carbon itself. The pillar has a larger surface area sideways, enabling more SE to escape from there and interact with adsorbed hydrocarbons on the pillars, resulting in further lateral growth [45]. Despite this, lateral growth is not an ongoing process, as it will eventually saturate, as shown in Fig. 3(c). Theoretically, it will saturate once the C-pillar volume exceeds the e-beam interaction volume. Practically, it will saturate sooner due to the continuous energy loss of electrons, meaning that electrons in some far away regions of the interaction volume do not have enough energy to produce SE, or the SE have insufficient energy to escape the C-pillars.

Further, the Fig. 6(d) suggests that the C-pillar width size should be larger at higher kVs, but Fig. 3(c–e) show an opposite trend. This behaviour is undoubtedly impacted by SEY relative to e-beam energy, but another fundamental aspect of e-beam interaction with solids could also play a role, which is the change of e-beam shape from cylindrical near the surface to conical and finally becoming almost spherical as it propagates through the material. To visualize these shape profile changes, we simulate the e-beam interaction with a two-layer system: C (500 nm thick) and $AuCl_3$(1000 nm), for 3 and 30 kV, shown in Fig. S4 of the SI. For a 3 keV e-beam, the shape of the e-beam 50 nm under the surface of the carbon layer is conical in the central part, but electrons are also scattered sideways (see Fig. S4(a)). In contrast, it takes a spherical shape if observed 500 nm in the z-direction (Fig. S4(b)). For 30 kV, the dominant shape is conical for both 50 and 500 nm under the carbon layer surface, with only a few electrons scattering sideways, as is shown in Fig. S4(c–d). As the e-beam energy increases, it becomes concentrated along the central axis of irradiation, thereby decreasing its impact, particularly regarding the lateral evolution of the C-pillar.

So far, the discussion has been focused on the horizontal profile of C-pillars, but they also extend vertically. The measurements of C-pillar height shown in Fig. S3 reveal that vertical growth will carry on linearly relative to increasing e-beam energy. The top of the C-pillars has a round shape, and its diameter is larger than that of the e-beam. The SE produced in the top area will contribute to height growth, as hydrocarbons recently adsorbed or in a gas state close to the top of the pillars will constantly dissociate from the SE of both types produced in the C-pillars. The SEY decreases with increasing e-beam energy, implying that the C-pillars' vertical dimensions should be smaller at higher e-beam energy. However, the experimental observations (Fig. 3(e) and S3) do not support this claim. Here, we propose a solution to this contradiction by analysing, via simulation, the behaviour of BSE (a source of SE-II). As mentioned earlier, the growth of C-pillars occurs in situ during irradiation. We simulated the growth of C-pillars by adding five carbon layers with thicknesses of 10, 50, 250, 500, and 5000 nm (bulk) on top of an $AuCl_3$ crystal, which itself has a thickness of 5000 nm. The simulation had two parts: first, we obtained the values of the BSE coefficient only from the $AuCl_3$ crystal, and afterwards, the carbon layers were added. In this manner, it was possible to track the impact of increasing the carbon layer on the BSE yield of the system. The Fig. 7 summarizes the results of these simulations graphically, revealing that when C-pillar reach 10 nm height, in the 1–3 keV range, the BSE originate from both carbon deposition and $AuCl_3$ crystal, and from 5 keV to 30 keV almost all BSE comes from $AuCl_3$ as the values are similar for single system [$AuCl_3$(5000 nm)] and two-layer system [C(10 nm)-$AuCl_3$(5000 nm)]. As the carbon deposition continues to grow, more and more BSEs originate from carbon nanostructures, which explains the decrease of growth after the carbon pillar reaches 500 nm height.

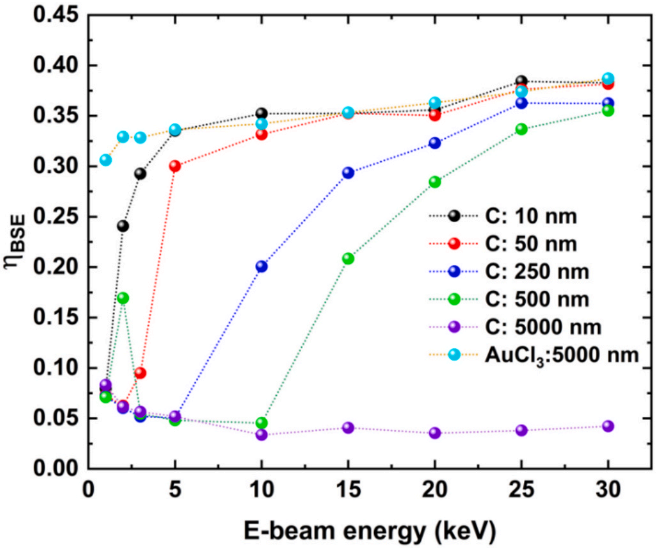

Fig. 7. The variation of simulated BSE coefficient values for $AuCl_3$, for the 1–30 keV range, and after the addition of a different thickness of carbon layer on top of the $AuCl_3$ crystal.

We observe that in bulk carbon (5000 nm), the value of the η_{BSE} is minimal and decreases slowly from 1 to 5 keV, after which it remains constant and does not depend on the e-beam energy. In this regard, the vertical growth of the C-pillar will saturate once the BSE originates within itself. The maximum depth of carbon bulk from which electrons backscatter is ~3000 nm. We treated the BSE here as a source of SE-II, and from these results, we see that the BSE increases rapidly in the 1–5 keV range and then very slowly from 5-30 keV. Thus, the SE-II yield will follow the trend of η_{BSE} by increasing relative to e-beam energy until it reaches a value that represents the properties of carbon bulk nanostructures. This behaviour of BSE explains the experimental results shown in Fig. 3(e), where the C-pillar increases as the e-beam energy increases from low to high.

4.2. Near-surface decomposition of $AuCl_3$ crystal

The carbon-deposited nanostructures hinders the under-surface alternation of gold chloride crystals, as signalled by EDS analysis and Cl/Au ratio variation, and visualised by FIB cross-section. The interaction of e-beam with the crystal bulk induces decomposition of gold chloride, resulting in mass loss (voids) and Au NP formation. The Au NPs are concentrated near the surface, while the voids are extended both horizontally and vertically inside the crystal bulk. Voids impose detrimental effects on the properties of materials [46], and their formation mechanism is treated using two inelastic-origin interaction effects: thermal effects and radiolysis.

The inelastic interaction of electrons with the crystal converts a part of the energy into heat [46,47]. There are several models [48–50] established to estimate the temperature rise in solid samples due to intense e-beam irradiation. In our work, the temperature rise in a stationary probe for thick samples was assessed using the Reimer model [36,51]:

$$\Delta T = \frac{1.5}{\pi}\frac{IU}{\kappa R}\left[K\right] \tag{2}$$

where I is the beam current (A), U the accelerating voltage (V), R the electron interaction range (m) within the sample bulk, and κ is the thermal conductivity (W/m•K). The thermal conductivity of $AuCl_3$ is not determined theoretically or measured accurately (see section S4 of the SI for more details). The temperature rise estimated for $AuCl_3$, according to Eq. (2), is given in Fig. 8 (in Table S2 and Fig. S6 of the SI, the

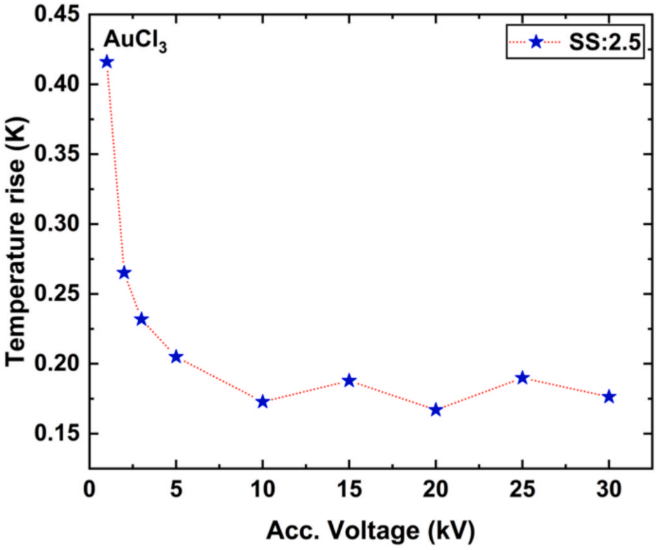

Fig. 8. The temperature rise relative to increasing acc. voltage for $AuCl_3$ crystal ($\kappa = 1.0W/m \bullet K$) according to the Reimer model.

temperature rise estimations for other conditions are provided). The temperature rise was also estimated for an extended range of thermal conductivity 0.1–5.0 W/m•K for $AuCl_3$ (see Table S3 and Fig. S7 of SI). Based on these calculations, the temperature rise due to $AuCl_3$ crystal electron irradiation, for the spot size 2.5, is < 6.0 K. Similar values of temperature rise are also obtained for C-pillars. Based on these results, the thermal effects are considered negligible in the mechanism behind sample decomposition. This conclusion is also derived from the fact that the spatial profile of the voids does not match the profile of the temperature rise relative to increasing acceleration voltage. The Reimer model implies a higher temperature for the lower kV range (the amount of inelastic interaction scales inversely with the increasing energy of incident electrons). On the other hand, voids have smaller spatial dimensions in that voltage range.

The radiolytic mechanism involves the inelastic transfer of energy from incident electrons to the $AuCl_3$ crystal, primarily causing Au–Cl bond breakage. Following bond disruption, chlorine (Cl or Cl_2) escapes as a gas under the SEM vacuum, while gold atoms agglomerate into nanoparticles concentrated near the crystal surface. This mass loss, through chlorine release and Au nanoparticle formation, produces voids within the crystal bulk.

Interestingly, voids formed under 10 kV irradiation are larger than those under 15 kV, while no voids are observed under 20 or 30 kV irradiation. This indicates that void growth is not directly proportional to the electron beam interaction volume. Given the poor electrical conductivity of $AuCl_3$, inelastic interactions deposit energy predominantly in the form of secondary electrons. Those generated in deeper regions cannot escape, leading to charge accumulation and the formation of local electric fields—sometimes referred to as a "Coulomb explosion" [52]—which drive further bond breakage and atomic migration. These local electric fields enhance radiolysis and act more as *shape-defining* factors for voids.

Additional factors such as crystal surface imperfections and long exposure times can further influence void morphology. Monte Carlo simulations assume that the electron beam strikes a perfectly flat surface at normal incidence, which does not always reflect real conditions. Irregular surface profiles alter electron scattering trajectories, while prolonged beam exposure may cause beam drift, distorting the shape of C-pillars and the voids beneath. Together, these three factors act as *morphology-defining* influences.

Overall, we regard deposited energy as the most critical factor shaping void formation. To quantitatively support this assumption, we analyzed deposited energy as a function of incident beam energy using theoretical models and simulations.The theoretical model proposed by Kanaya et al. [53,54] was used to estimate the deposition energy E_A using the following simple relationship:

$$E_A = E_0 - \eta_T E_T - \eta_{BSE} E_{BSE} [eV] \tag{3}$$

where E_0 is the energy of incident electrons, E_{BSE} is the energy of backscattering electrons, E_T is the energy of electrons transmitted from a certain depth x of the sample, and η_T is the electron transmission coefficient. The values of E_{BSE} and η_{BSE} are obtained from simulations (see section S5 of the SI). On the other hand, the values of E_T and η_T are calculated using the following equation:

$$E_T = (1-y)^{\frac{3}{5}} E_0 [eV] \tag{4}$$

where $y = x/R$ is known as reduced depth of electron penetration (R is the range of electron interaction [nm]), and:

$$\eta_T = exp\left(-\frac{\gamma x}{R-x}\right) \tag{5}$$

where $\gamma = 0.187Z^{2/3}$ (Z is the atomic number and is taken as the average value of Au and Cl atomic numbers). The value of x is chosen to be 350 nm under the surface, as the decomposition mainly occurs within this range.

By combining the simulations and theoretical calculations results, the values of all parameters in Eq. (3) were ultimately obtained to estimate the deposited energy in the $AuCl_3$ sample relative to the e-beam energy shown graphically in Fig. 9. This graph shows that the deposited energy increases in the range of 1–15 kV and decreases in the range 20–30 kV. The trend of deposition energy aligns strongly with the experimental observation of nanovoids' spatial growth dynamics, with the two largest voids occurring under irradiation spots of 10 and 15 kV.

The positive value of deposited energy for 20 kV implies that a void must be present, but Fig. 5 indicates no voids directly under 20 or 30 kV irradiation spots. As the FIB cross-section cuts continue in the *y-axis* direction, the voids appear also under 20 and 30 kV, as shown in Fig. S9 (a-b). This interesting behaviour means that for the voids to occur, the electrons must be deposited near the surface. Electrons accelerated at 20 kV or higher are very energetic, and their inelastic interaction has a lower probability of initiating decomposition immediately under the surface of the irradiation spot. The electrons also spread laterally, so they will lose energy and be deposited away from the irradiation spot but still near the surface to initiate void formation.

The voids grow more in the horizontal direction. The void under 10 kV is ~850 nm wide and 520 nm deep, a result also observed in simulations (Fig. 10(a)), which show that electrons scatter more laterally than forward as the energy increases due to the screening effect. The wider size of the voids favours the second mechanism because the heat generated through the sample tends to distribute radially [48] from its source, resulting in a more symmetrical shape. The voids observed here favour randomly scattering events depending on the energy distribution through the bulk.

The appearance of the voids reveals an interesting interplay between electrons and voids, as the electrons deposit energy that impacts the formation and growth of the voids, and the voids, in turn, affect their scattering dynamics through the crystal. Fig. 10(a) shows a direct comparison of the real thickness of the sample under each irradiation spot and the simulated depth and lateral interaction of the e-beam. This figure indicates that electrons from the beam with an energy of 20 keV or lower cannot be transmitted through the crystal; consequently, the EDS spectra at 10 and 15 kV would not show a silicon peak. On the other hand, the zoomed EDS in Fig. 10(b) shows a peak of silicon formed at 10 keV after 600 s. In contrast, the higher peak is visible in the zoomed EDS

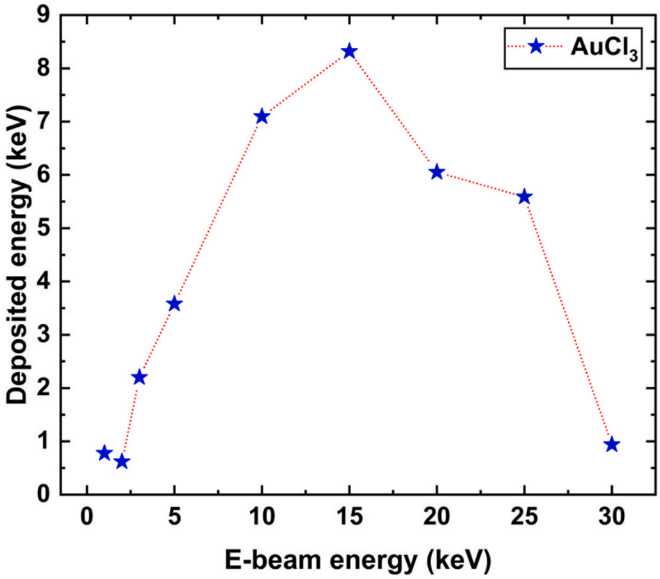

Fig. 9. The deposited energy over e-beam energy in the of $AuCl_3$ crystal according to Kanaya model.

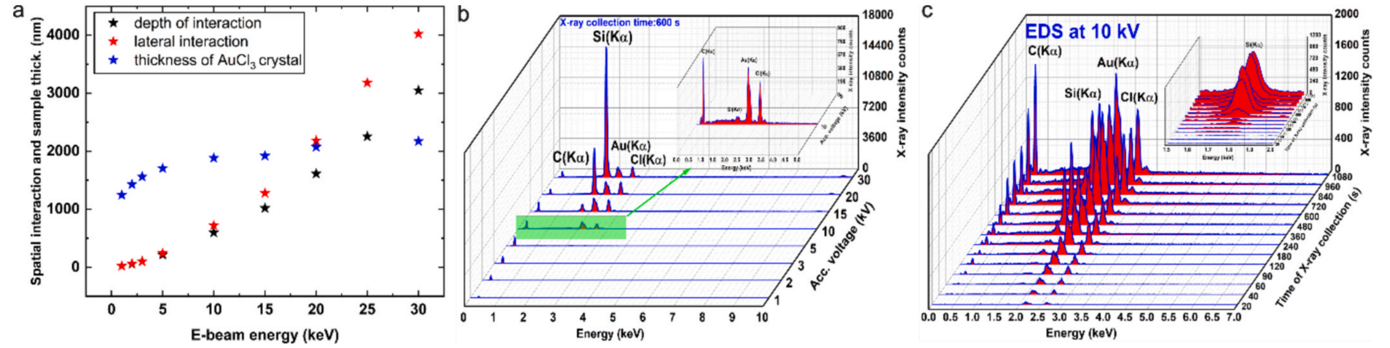

Fig. 10. (a) Spatial dimensions of e-beam interaction with $AuCl_3$ crystal and its real thickness under irradiation spot. (b) EDS spectra collected at 10 kV, for 10 min irradiation, where the zoomed graph inset reveal the initial stage of silicon intensity peak formation. (c) EDS at 10 kV collected in the 20–1080 s time interval. The zoomed graph shows a larger intensity peak for silicon.

inset of Fig. 10(c), which shows the variation of silicon X-ray intensity for different irradiation times. In further investigation of this issue, we simulated the voids at 15 kV e-beam (see section S7 of SI). Fig. S10(a) shows simulations of a 350 nm thick void in a 15 kV field, which allows electrons to reach the silicon with sufficient energy to generate a characteristic X-ray of silicon in the K_α transition. In contrast, Fig. S10(b) shows that when voids are not simulated, electrons are localized entirely inside the sample.

The energy of these local electric fields induced within the $AuCl_3$ bulk is sufficient to overcome the Au-Cl energy barrier (approximately 2.8 ± 0.2 eV) and dissociate it, with the heavy Au atoms remaining in the material. In contrast, the Cl atoms diffuse through the crystal or escape from it. After dissociation, the Au^{3+} will capture free electrons and reduce to Au^0. Around 10^3 incident electrons are necessary to reduce Au^{3+} to Au^0 [55]. The Au atoms are heavy, and the incident electrons in the range 1–30 keV cannot transfer enough momentum to move them through the sample structure and start coalescence. In this regard, the local electric field will interact with the Au atoms, thereby impacting their charge symmetry distribution, which will result in their electron clouds overlapping and bonding together. As the gold atoms start to synthesize into Au NP, the surface free energy will decrease, thus enhancing their thermodynamic stability.

In summary, the use of e-beam to tailor material properties at the nanoscale poses a challenge due to the possibility of damage. In our study, a gold chloride crystal was subjected to intense e-beam irradiation in the 1–30 kV range of the SEM. The interaction of the e-beam with the crystal yielded two significant results: firstly, carbon deposited on the crystal surface as a pillar nanostructure; secondly, the under-surface bulk of the crystal decomposed, leading to void formation and the creation of Au nanoparticles under the irradiation spots.

5. Conclusions

In this paper, we demonstrate the impact of electron beams accelerated in the range of 1–30 kV on a solid gold chloride sample. This sample exhibits considerable e-beam damage sensitivity within this interaction range. The first effect of the e-beam is the dissociation of environmental or adsorbed hydrocarbons, resulting in carbon deposition on the sample surface in a pillar-like shape. These pillar-shaped carbon nanostructures increase in both vertical and horizontal directions, with height surpassing lateral growth. The width of the C-pillars decreases with increasing e-beam energy and exhibits a clear tendency to saturate with extended irradiation.

On the other hand, the vertical growth exhibits a linear trend, and generally, the height of the C-pillars increases with kV. The incident electrons initiate dissociation and depositions, but it is SE that are directly involved in their spatial growth, with BSE playing an indirect role. The second effect of the e-beam on the sample is that the near-surface of the crystal is decomposed, as the surface proximity provides a path for the diffusion and evacuation of volatile elements from the bulk of the crystal. The alternation of Cl/Au ratio, particularly observed in 15 and 30 kV, indicated that the decomposition of Au-Cl results in the diffusion out of the volatile component. At the same time, the non-volatile remains in the crystal and agglomerates into Au NP concentrated near the surface. The mass loss during the decomposition results in voids, with the most significant void occurring under 10 kV irradiation. In the range of 1–15 kV, voids are created directly under the irradiation spot; however, they can also be induced away from the irradiation spot, as observed for 20–30 kV. The spatial evolution dynamics of voids and their irregular shape (wider than deeper) do not fit with the assumption of a thermal effects mechanism; rather, it is radiolysis the main mechanism behind void formation, enhanced by three additional *morphology-defining* factors: local electric fields, crystal surface imperfections, and electron beam drift caused by long exposure times. The interaction of an e-beam with a crystal exhibits an interplay of electrons that alters the on- and near-surface dynamics of the crystal during the deposition of carbon and its subsequent decomposition, which occurs concurrently. These alterations subsequently impact the dynamics of electron interaction with the sample, as revealed by EDS analysis.

CRediT authorship contribution statement

Ibrahim Hameli: Writing – review & editing, Writing – original draft, Visualization, Validation, Investigation, Formal analysis, Data curation, Conceptualization. **Vasyl Shvalya:** Writing – review & editing, Writing – original draft, Visualization, Validation, Supervision, Investigation, Formal analysis, Data curation, Conceptualization. **Neelakandan M. Santhosh:** Writing – review & editing, Supervision, Formal analysis, Data curation, Conceptualization. **Ardita Kurtishaj Hamzaj:** Investigation, Formal analysis, Data curation. **Oleg Baranov:** Formal analysis, Conceptualization. **Uroš Cvelbar:** Writing – review & editing, Methodology, Conceptualization. **Janez Zavašnik:** Writing – review & editing, Validation, Supervision, Methodology, Investigation, Data curation, Conceptualization.

Declaration of competing interest

The authors declare that they have no known competing financial interests or personal relationships that could have appeared to influence the work reported in this paper.

Acknowledgements

Authors acknowledge the financial support from Public Agency for Scientific Research and Innovation Activity of the Republic of Slovenia

(ARIS), P1-0417, J2-4440, J2-50066. OB acknowledges the support from the project funded by the Ministry of Education and Science of Ukraine, under grant id. M/45- 2025, and the NATO Science for Peace and Security Programme under grant id. G7918 project AEGIS. JZ acknowledge the support from European Innovation Council Pathfinder project ThermoDust, grant agreement No. 101046835.

Appendix A. Supplementary data

Supplementary data to this article can be found online at https://doi.org/10.1016/j.apsusc.2025.164623.

Data availability

Data will be made available on request.

References:

[1] M. Ilett, M. S'ari, H. Freeman, Z. Aslam, N. Koniuch, M. Afzali, J. Cattle, R. Hooley, T. Roncal-Herrero, S.M. Collins, N. Hondow, A. Brown, R. Brydson, Analysis of complex, beam-sensitive materials by transmission electron microscopy and associated techniques, Philos. Trans. R. Soc. A Math. Phys. Eng. Sci. 378 (2020) 20190601, https://doi.org/10.1098/rsta.2019.0601.

[2] H. Gu, G. Li, C. Liu, F. Yuan, F. Han, L. Zhang, S. Wu, Considerable knock-on displacement of metal atoms under a low energy electron beam, Sci. Rep. 7 (2017) 184, https://doi.org/10.1038/s41598-017-00251-3.

[3] N. Jiang, Damage by induced electric field in beam-sensitive materials, Microsc. Microanal. 23 (2017) 1812–1813, https://doi.org/10.1017/S1431927617009722.

[4] N. Jiang, Beam damage by the induced electric field in transmission electron microscopy, Micron 83 (2016) 79–92, https://doi.org/10.1016/j.micron.2016.02.007.

[5] N. Jiang, Damage mechanisms in electron microscopy of insulating materials, J. Phys. D Appl. Phys. 46 (2013) 305502, https://doi.org/10.1088/0022-3727/46/30/305502.

[6] S.J. Randolph, J.D. Fowlkes, P.D. Rack, Effects of heat generation during electron-beam-induced deposition of nanostructures, J. Appl. Phys. 97 (2005), https://doi.org/10.1063/1.1942627.

[7] J. Holm, Quantifying low-keV beam damage in ultrathin MFI zeolite nanosheets with an SEM, Microsc. Microanal. 29 (2023) 131–137, https://doi.org/10.1093/micmic/ozac010.

[8] S. Suzuki, Low-energy irradiation damage in single-walled carbon nanotubes, in: Electronic Properties of Carbon Nanotubes, InTech, 2011. https://doi.org/10.5772/18140.

[9] B. Liu, Y. Hua, Z. Dong, P.K. Tan, Y. Zhao, Z. Mo, J. Lam, Z. Mai, The overview of the impacts of electron radiation on semiconductor failure analysis by SEM, FIB and TEM, in: 2018 IEEE International Symposium on the Physical and Failure Analysis of Integrated Circuits (IPFA), IEEE, 2018: pp. 1–6. https://doi.org/10.1109/IPFA.2018.8452485.

[10] C.W. Price, P.L. McCarthy, Low-voltage scanning electron microscopy of low-density materials, Scanning 10 (1988) 29–36, https://doi.org/10.1002/sca.4950100106.

[11] C. Fager, M. Röding, A. Olsson, N. Lorén, C. von Corswant, A. Särkkä, E. Olsson, Optimization of FIB–SEM tomography and reconstruction for soft, porous, and poorly conducting materials, Microsc. Microanal. 26 (2020) 837–845, https://doi.org/10.1017/S1431927620001592.

[12] R.F. Egerton, Radiation damage to organic and inorganic specimens in the TEM, Micron 119 (2019) 72–87, https://doi.org/10.1016/j.micron.2019.01.005.

[13] R.F. Egerton, Mechanisms of radiation damage in beam-sensitive specimens, for TEM accelerating voltages between 10 and 300 kV, Microsc. Res. Tech. 75 (2012) 1550–1556, https://doi.org/10.1002/jemt.22099.

[14] D.C. Joy, C.S. Joy, Dynamic charging in the low voltage SEM, Microsc. Microanal. 1 (1995) 109–112, https://doi.org/10.1017/S1431927695111095.

[15] M.A. Stevens Kalceff, G.J. Thorogood, K.T. Short, Charge trapping and defect segregation in quartz, J. Appl. Phys. 86 (1999) 205–208, https://doi.org/10.1063/1.370718.

[16] M.A. Stevens-Kalceff, K.J. Levick, The assessment of microscopic charging effects induced by focused electron and ion beam irradiation of dielectrics, Microsc. Res. Tech. 70 (2007) 195–204, https://doi.org/10.1002/jemt.20399.

[17] J. Cazaux, Charging at the steady state in EPMA, SEM and ESEM, Microsc. Microanal. 8 (2002) 426–427, https://doi.org/10.1017/S143192760210095X.

[18] J. Holm, STEM-in-SEM imaging and diffraction with extremely beam sensitive ultrathin zeolites, Microsc. Microanal. 27 (2021) 1584–1585, https://doi.org/10.1017/S1431927621005833.

[19] M. Hugenschmidt, K. Adrion, A. Marx, E. Müller, D. Gerthsen, Electron-beam-induced carbon contamination in STEM-in-SEM: quantification and mitigation, Microsc. Microanal. 29 (2023) 219–234, https://doi.org/10.1093/micmic/ozac003.

[20] H.W. Conru, P.C. Laberge, Oil contamination with the SEM operated in the spot scanning mode, J. Phys. E 8 (1975) 136–138, https://doi.org/10.1088/0022-3735/8/2/021.

[21] J. Hillier, On the investigation of specimen contamination in the electron microscope, J. Appl. Phys. 19 (1948) 226–230, https://doi.org/10.1063/1.1715049.

[22] R. Vane, V. Carlino, Environmental contamination sources and control in high resolution scanning electron microscopy, Microsc. Microanal. 11 (2005), https://doi.org/10.1017/S1431927605501661.

[23] A.F.G. Leontowich, A.P. Hitchcock, Secondary electron deposition mechanism of carbon contamination, J. Vacuum Sci. Technol. 30 (2012), https://doi.org/10.1116/1.3698602.

[24] N. Silvis-Cividjian, C.W. Hagen, L.H.A. Leunissen, P. Kruit, The role of secondary electrons in electron-beam-induced-deposition spatial resolution, Microelectron. Eng. 61 (2002) 693–699.

[25] J. Hollenshead, L. Klebanoff, Modeling radiation-induced carbon contamination of extreme ultraviolet optics, J. Vacuum Sci. Technol. 24 (2006) 64–82, https://doi.org/10.1116/1.2140005.

[26] M. Antognozzi, A. Sentimenti, U. Valdrè, Fabrication of nano-tips by carbon contamination in a scanning electron microscope for use in scanning probe microscopy and field emission, Microsc. Microanal. Microstruct. 8 (1997) 355–368, https://doi.org/10.1051/mmm:1997127.

[27] K. Kanayat, S. Okayama, Penetration and energy-loss theory of electrons in solid targets, J. Phys. D Appl. Phys. 5 (1972) 43.

[28] P. Hovington, D. Drouin, R. Gauvin, CASINO: a new Monte Carlo code in C language for electron beam interaction - Part I: Description of the program, Scanning 19 (1997) 1–14, https://doi.org/10.1002/sca.4950190101.

[29] D. Drouin, A.R. Couture, D. Joly, X. Tastet, V. Aimez, R. Gauvin, CASINO V2.42 - a fast and easy-to-use modeling tool for scanning electron microscopy and microanalysis users, Scanning 29 (2007) 92–101, https://doi.org/10.1002/sca.20000.

[30] S. Srivastava, M. Haridas, J.K. Basu, Optical properties of polymer nanocomposites, Bull. Mater. Sci. 31 (2008) 213–217, https://doi.org/10.1007/s12034-008-0038-9.

[31] A. Usher, D.C. McPhail, J. Brugger, A spectrophotometric study of aqueous Au(III) halide–hydroxide complexes at 25–80°C, Geochim. Cosmochim. Acta 73 (2009) 3359–3380, https://doi.org/10.1016/j.gca.2009.01.036.

[32] Sun-Jong Lim, Chan-Hong Lee, Analysis of probe current in scanning electron microscopy, in: International Conference on Control, Automation and Systems, Seoul, Korea, 2008: pp. 1200–1203.

[33] B.-P. Song, R.-D. Zhou, G.-Q. Su, H.-B. Mu, G.-J. Zhang, R.-A. Bu, Time evolution of secondary electron emission and trapped charge accumulation in polyimide film under various primary electron irradiation currents, Appl. Surf. Sci. 390 (2016) 346–349, https://doi.org/10.1016/j.apsusc.2016.07.179.

[34] T.E. Everhart, P.H. Hoff, Determination of kilovolt electron energy dissipation vs penetration distance in solid materials, J. Appl. Phys. 42 (1971) 5837–5846, https://doi.org/10.1063/1.1660019.

[35] K.F. Galloway, P. Roitman, Important considerations for SEM total dose testing, IEEE Trans. Nucl. Sci. 24 (1977) 2066–2070, https://doi.org/10.1109/TNS.1977.4329166.

[36] R.F. Egerton, P. Li, M. Malac, Radiation damage in the TEM and SEM, Micron (2004) 399–409, https://doi.org/10.1016/j.micron.2004.02.003.

[37] D.C. Joy, S. Luo, An empirical stopping power relationship for low-energy electrons, Scanning 11 (1989) 176–180.

[38] T. Susi, J.C. Meyer, J. Kotakoski, Quantifying transmission electron microscopy irradiation effects using two-dimensional materials, Nat. Rev. Phys. 1 (2019) 397–405, https://doi.org/10.1038/s42254-019-0058-y.

[39] A.J.V. Griffiths, T. Walther, Quantification of carbon contamination under electron beam irradiation in a scanning transmission electron microscope and its suppression by plasma cleaning, in: J. Phys. Conf. Ser, Institute of Physics Publishing, 2010, https://doi.org/10.1088/1742-6596/241/1/012017.

[40] M.B. Matthews, S.L. Kearns, B. Buse, Electron beam-induced carbon erosion and the impact on electron probe microanalysis, Microsc. Microanal. 24 (2018) 612–622, https://doi.org/10.1017/S1431927618015398.

[41] N. Silvis-Cividjian, C.W. Hagen, P. Kruit, Spatial resolution limits in electron-beam-induced deposition, J. Appl. Phys. 98 (2005), https://doi.org/10.1063/1.2085307.

[42] W.F. van Dorp, C.W. Hagen, A critical literature review of focused electron beam induced deposition, J. Appl. Phys. 104 (2008), https://doi.org/10.1063/1.2977587.

[43] K. Uesugi, T. Yao, Nanometer-scale fabrication on graphite surfaces by scanning tunneling microscopy, Ultramicroscopy 42–44 (1992) 1443–1445, https://doi.org/10.1016/0304-3991(92)90463-T.

[44] J.D. Fowlkes, S.J. Randolph, P.D. Rack, Growth and simulation of high-aspect ratio nanopillars by primary and secondary electron-induced deposition, J. Vacuum Sci. Technol. 23 (2005) 2825–2832, https://doi.org/10.1116/1.2101732.

[45] N. Silvis-Cividjian, C.W. Hagen, P. Kruit, M.A.J.v.d. Stam, H.B. Groen, Direct fabrication of nanowires in an electron microscope, Appl. Phys. Lett. 82 (2003) 3514–3516, https://doi.org/10.1063/1.1575506.

[46] M. Liu, L. Xu, X. Lin, Heating effect of electron beam bombardment, Scanning 16 (1994) 1–5.

[47] H. Guo, P. Zhou, D. Natelson, J. Lou, Quantification of electron beam heating effect in TEM, Microsc. Microanal. 23 (2017) 1766–1767, https://doi.org/10.1017/s1431927617009497.

[48] Z. Wang, L. Gui, D. Han, Z. Xu, L. Han, S. Xu, Measurement and evaluation of local surface temperature induced by irradiation of nanoscaled or microscaled electron beams, Nanoscale Res. Lett. 14 (2019) 31, https://doi.org/10.1186/s11671-018-2821-x.

[49] F. Niekiel, S.M. Kraschewski, J. Müller, B. Butz, E. Spiecker, Local temperature measurement in TEM by parallel beam electron diffraction, Ultramicroscopy 176 (2017) 161–169, https://doi.org/10.1016/j.ultramic.2016.11.028.

[50] A. Nouiri, S. Chaguetmi, N. Belabed, Monte Carlo model of the temperature rise at a GaAs surface under an electron beam, Surf. Interface Anal. 38 (2006) 1153–1157, https://doi.org/10.1002/sia.2372.

[51] L. Reimer. Scanning Electron Microscopy-Physics of image formation and microanalysis, Springer Berlin Heidelberg, Berlin Heidelberg, 1998, https://doi.org/10.1007/978-3-540-38967-5.

[52] W. Feng, T. Gemming, L. Giebeler, J. Qu, K. Weinel, L.A. Jácome, B. Büchner, I. Gonzalez-Martinez, Influence of magnetic field on electron beam-induced Coulomb explosion of gold microparticles in transmission electron microscopy, Ultramicroscopy 262 (2024) 113978, https://doi.org/10.1016/j.ultramic.2024.113978.

[53] K. Kanaya, S. Ono, K. Kanayat, S. Okayama, Penetration and energy-loss theory of electrons in solid targets, J. Phys. D Appl. Phys. 5 (1972) 43.

[54] K. Kanaya, S. Ono, The energy dependence of a diffusion model of an electron probe into solid targets, J. Phys. D Appl. Phys. 11 (1978) 1495.

[55] J.H. Park, N.M. Schneider, J.M. Grogan, M.C. Reuter, H.H. Bau, S. Kodambaka, F. M. Ross, Control of electron beam-induced Au nanocrystal growth kinetics through solution chemistry, Nano Lett. 15 (2015) 5314–5320, https://doi.org/10.1021/acs.nanolett.5b01677.